

# Polylidar - Polygon Extraction from Triangular Meshes\*

Jeremy Castagno<sup>1</sup> and Ella Atkins<sup>2</sup>

**Abstract**—This paper presents Polyli<sup>2</sup>dar, an efficient algorithm to extract non-convex polygons from 2D point sets. Polyli<sup>2</sup>dar is able to extract multiple disjoint polygons and capture interior holes. The algorithm begins by triangulating the point set and filtering triangles by user configurable parameters such as triangle edge length. Next, connected triangles are extracted into triangular meshes representing the shape of the point set. The key to Polyli<sup>2</sup>dar’s speed, and the main contribution of this paper, is in efficiently transforming each triangular mesh into a concave polygon. This paper describes Polyli<sup>2</sup>dar and provides benchmarks to comparatively evaluate its speed and accuracy. Results show good accuracy and  $\sim 4$  times speedup compared to other concave polygon extraction methods.

## I. INTRODUCTION

Video and LiDAR data are widely used in robotics to provide rich information about the environment. LiDAR generates point clouds used for localization and mapping [1], 3D modelling [2], and scene classification for autonomous navigation [3]. For simplified scene reconstruction, point clouds can be transformed to irregular triangular meshes (ITM) to identify drivable surfaces and obstacles for self-driving vehicles [4], [5]. Unmanned Aerial Vehicles (UAVs) also need simplified representations of operating regions for navigation and landing [6], [7], particularly in complex urban regions. Surfaces such as flat rooftops can offer safe nearby landing zones once planarity/shape is determined [8], [9].

Robotic systems often simplify 3D data to realistic 2D representations. For example a UAV flying at appreciable altitude can typically approximate buildings and vehicles as objects on a 2D plane. Objects represented as 2D point sets can then be processed to provide polygonal outlines for mapping and decision making. Robots operating indoor can similarly presume 2D models of wall and floor surfaces in hallways and other uncluttered spaces. Both applications can require robust and fast shape extraction from 2D point sets.

This paper presents Polyli<sup>2</sup>dar, an efficient algorithm to transform 2D point sets into simplified non-convex (i.e. concave) polygons. Polyli<sup>2</sup>dar begins by triangulating the point set and filtering triangles given user-specified parameters such as maximum triangle edge length. Once filtering is complete, connected triangles are individually extracted resulting in a set of triangular meshes representing the shape of the point set. Next, Polyli<sup>2</sup>dar rapidly transforms each triangular mesh into a valid concave 2D polygon excluding holes from the mesh. The algorithm and software presented

may be used to concisely represent the shape of 2D points as polygons with the option of holes.



Fig. 1. (a) Convex hull of a point set (red); (b) multipolygon extraction using Polyli<sup>2</sup>dar (green). Note that Polyli<sup>2</sup>dar also identifies the hole (orange).

We show the Polyli<sup>2</sup>dar algorithm is approximately 4 times faster than leading open source approaches for concave polygon extraction. Polyli<sup>2</sup>dar’s speed is attributed to rapidly identifying boundary edges by walking the hull of the mesh and handling edge cases to ensure a valid polygon is returned. Contributions of this paper are:

- A faster open source [10] concave (multi)polygon extraction algorithm from 2D point sets.
- A benchmark comparison of leading concave polygon extraction techniques in terms of accuracy and speed.

Below, Sections II and III provide background on non-convex shape generation and mathematical preliminaries, respectively. Section IV describes Polyli<sup>2</sup>dar algorithms, while Section V shows benchmark test results of Polyli<sup>2</sup>dar versus other methods. Section VI describes comprehensive Polyli<sup>2</sup>dar test results and Section VII concludes the paper.

## II. BACKGROUND

Characterizing the shape of a set of 2D points  $\mathcal{P}$  has been a long-term focus of computational geometry research. A convex hull is defined as the smallest convex polygon that fully encapsulates all points in a set  $\mathcal{P}$ . Although widely used to estimate shape, point sets with non-convex distributions are poorly characterized by a convex hull [11]. Convex hull over-estimation can be a serious issue when the points represent physical objects, e.g., clear rooftop landing regions. Several algorithms have been developed to construct shapes that “fit” or “cover” point sets more closely.

Figure 1 compares convex and concave hulls. Figure 1b is the multipolygon output of Polyli<sup>2</sup>dar described below. While there is a unique convex hull, there is no true or unique concave hull. Concave hull algorithm implementations can also have different output types. Some return only an unordered

\*This work was supported in part by NSF I/UCRC Award 1738714.

<sup>1</sup>Jeremy Castagno is a Robotics Institute PhD candidate, University of Michigan, jdcasta@umich.edu

<sup>2</sup>Ella Atkins is a Professor of Aerospace Engineering and Robotics, University of Michigan, ematkins@umich.edu

set of edges while others return a single polygon. Some algorithms return multiple disconnected polygons (multipolygon), and some can generate holes inside a polygon.

The  $\alpha$ -shape algorithm is an early strategy to generate a family of shapes ranging from a convex hull to a point set [12]. The parameter  $\alpha$  dictates the radius of a closed disk used to prune/remove area in the convex hull. This disk is allowed to move freely shaving off the excess shape until it finds points. When disk radius is large, ideally infinite, the convex hull is produced; when disk radius is infinitesimally small only the points remain. A common implementation of  $\alpha$ -shape organizes points using Delaunay triangulation and filters triangles whose circumcircle radius is less than  $\alpha$ . The final shape is then the union of the remaining edges and triangles. Note that the  $\alpha$ -shape method allows one to create multiple non-intersecting shapes with the possibility of holes.

The algorithm in [11] produces polygons from point sets called  $\chi$ -shapes. Like some  $\alpha$ -shape implementations, the  $\chi$ -shape approach begins with Delaunay triangulation to order and spatially connect data points. The algorithm differs by iteratively removing the longest exterior edges from triangulation based on a specified maximum length parameter  $l$ . A corner case occurs when edge removal results in a non-simple polygon, i.e., the polygon wraps into itself; in this case edge removal is skipped. The  $\chi$ -shape produced is a single polygon with no possibility of holes.

The geospatial software library Spatialite [13], an extension to SQLite [14], contains a concave hull extraction procedure. The algorithm again starts with Delaunay triangulation then analyzes the distribution of each triangle’s edge length to determine mean  $\mu_l$  and standard deviation  $\sigma_l$ . Any triangle with edge length greater than  $C \cdot \sigma_l + \mu_l$  is removed, where  $C$  is a user-defined parameter. The final geometry returned is the union of all triangles computed with GEOS, a high performance open source geometry engine. The output may be a multipolygon (i.e., multiple disjoint polygon regions) with the possibility of holes inside each.

PostGIS is a geospatial database of computational geometry routines such as the concave hull method in [15]. This algorithm first calculates the convex hull and then shrinks the hull by adjusting vertex connections to closer points which “cave in” the hull. This process recursively shrinks a boundary until a user-specified percent reduction in area from the convex hull is achieved. The resulting shape is a single polygon with the possibility of holes.

Table I provides a summary of the concave hull algorithms discussed above. The Computation Geometry Abstraction Library (CGAL) is used as the implementation of the  $\alpha$ -shape method [16]. Note that the time complexity of all algorithm implementations, with the exception of PostGIS, is  $\mathcal{O}(n \log n)$ . Our paper contributes a procedure to more rapidly compute (multi)polygon output with the possibility of holes. Though this is a complex output to generate, we show through benchmarks that our algorithm and implementation outperforms other available approaches.

TABLE I  
CONCAVE HULL EXTRACTION METHODS

Algorithm	Output	Holes?
CGAL $\alpha$ -shape	Unordered	Yes
	Set of Edges	
$\chi$ -shapes	Unordered	No
	Set of Edges	
Spatialite	(multi)polygon	Yes
PostGIS	polygon	Yes
Polylidar (new)	(multi)polygon	Yes

### III. PRELIMINARIES

A 2D *point set* is an arbitrarily ordered set of two dimensional points in a Cartesian reference frame. Each point is defined by orthogonal bases  $\hat{e}_x$  and  $\hat{e}_y$  with

$$\vec{p}_i = x \hat{e}_x + y \hat{e}_y = [x, y] \quad (1)$$

where  $x, y$  are plane coordinates.

An  $n$ -point array  $\mathcal{P} = \{\vec{p}_1, \vec{p}_2, \dots, \vec{p}_n\}$  contains points  $\vec{p}_i \in \mathbb{R}^2$  indexed by  $i$ . A triangular mesh  $\mathcal{T}$  is defined by

$$\mathcal{T} = \{t_1, t_i, \dots, t_k\} \quad (2)$$

where each  $t_i$  is a triangle with vertices defined by three point indices  $\{i_1, i_2, i_3\} \in [1, n]$  referencing points in  $\mathcal{P}$ .

We follow the Open Geospatial Consortium (OGC) standard [17] for defining *linear ring* and *polygon*. A linear ring is a consecutive list of points that is both closed and simple. This requires a linear ring to have non-intersecting line segments that join to form a closed path. The key components of a valid polygon are a single exterior linear ring representing the *shell* of the polygon and a set of linear rings (possibly empty) representing *holes* inside the polygon.

### IV. METHODS

Sections IV-A, IV-B, and IV-C describe the triangulation data structures, filtering, and mesh extraction respectively. Section IV-D describes polygon extraction while Section IV-E describes time complexity.

#### A. Triangulation with Half-Edge Decomposition

Polylidar begins with the Delaunator library [18] performing a Delaunay triangulation of point set  $\mathcal{P}$ . This library is unique in its speed and output data structure which returns a *half-edge* representation. Some triangulation implementations refer to a shared edge as  $A \leftrightarrow B$  while Delaunator decomposes this relationship further using two half-edges  $A \rightarrow B$  and  $B \rightarrow A$ . An example of this decomposition and resulting data structures is shown in Figure 2.

Figure 2a triangulates point set  $\{\text{PI0, PI1, PI2, PI3}\}$ . Triangulation produces two triangles,  $t_0$  and  $t_1$ , with half-edges  $\{\text{HE0, HE1, HE2}\}$  and  $\{\text{HE3, HE4, HE5}\}$ , respectively. Each half-edge supports clockwise travel to the next half-edge in that triangle’s edge set. Figure 2b lists the resulting *halfedges*, *triangles*, and *points* data structures. The *halfedges* array is indexed by a half-edge reference id. It provides the opposite half-edge of a shared edge if it exists; otherwise -1 is returned. The *triangles* array is also

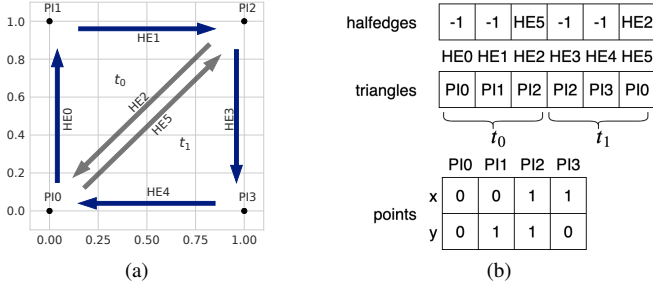


Fig. 2. (a) Triangulation of a square point set using Delaunay [18] with output data structure indexed by half edge ids in (b). HE=half edge, PI=point index,  $t$ =triangle. Grey edges show shared edges decomposed individually.

indexed by half-edge id and gives the starting point index of the associated half edge. The relationship between half-edge and triangle indices is  $t = \text{floor}(he/3)$ .

### B. Triangle Filtering

As with Spatialite and  $\alpha$ -shape methods the initial shape starts with  $k$  triangles in  $\mathcal{T}$  per Eqn. 2 returned from Delaunay triangulation. Also similar to  $\alpha$ -shape and Spatialite methods, Polyliar filters triangles by configurable criteria for each triangle. Polyliar allows the user to perform triangle filtering using either the  $\alpha$  parameter or maximum triangle edge length parameter  $l_{max}$ . The filtered triangle set is denoted  $\mathcal{T}_f$ . Algorithm 1 outlines the triangle filtering process when filtering by triangle edge length.

#### Algorithm 1: Triangle Filtering

**Input** : Triangles:  $\mathcal{T}$ , Point Cloud:  $\mathcal{P}$ ,  $l_{max}$

**Output**: Filtered Triangle Set,  $\mathcal{T}_f$

- 1  $\mathcal{T}_f = \emptyset$
- 2 **for**  $t_i$  **in**  $\mathcal{T}$ :
- 3      $l_{max,i} = \text{MaxTriangleEdgeLength}(t_i)$
- 4     **if**  $l_{max,i} < l_{max}$ :
- 5          $\mathcal{T}_f = \mathcal{T}_f + t_i$
- 6 **return**  $\mathcal{T}_f$

### C. Triangular Mesh Region Extraction

An iterative plane extraction procedure inspired from [19] generates subsets of  $\mathcal{T}_f$  that are spatially connected. These subsets are denoted  $\mathcal{T}_r$  which represent triangular mesh regions. A spatial connection between triangles exists when they share an edge. A random seed triangle is selected from  $\mathcal{T}_f$  where a new region is created and expanded by its adjacent edge neighbors from the halfedge data structure. Region growth halts when no more triangles in  $\mathcal{T}_f$  connect to the region. The process repeats with another seed triangle until all triangles in  $\mathcal{T}_f$  have been examined.

Figure 3a shows triangular mesh region examples. Distinct regions are shown in orange and blue; light grey edges denote triangles that have been filtered out. The output of this step is a set of spatially connected triangular mesh regions,  $\mathcal{T}_R$ , where each specific region,  $\mathcal{T}_{r,i}$ , is a set of triangle indices. We denote the set of  $k$  triangular mesh regions as:

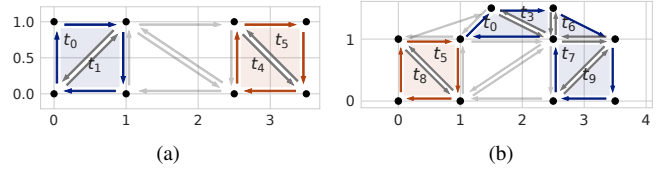


Fig. 3. (a) Example of two regions extracted denoted by orange and blue. Triangles  $t_0$  and  $t_1$  are one region while  $t_4$  and  $t_5$  are another. (b) Two regions are also extracted even with a shared vertex.

$$\mathcal{T}_R = \{\mathcal{T}_{r,1}, \mathcal{T}_{r,i}, \dots, \mathcal{T}_{r,k}\} \quad (3)$$

$$\mathcal{T}_{r,i} = \{t_i, \dots, t_j\} \quad (4)$$

### D. 2D Polygon Extraction

Polygon extraction has three steps: data structure initialization, concave shell extraction, and hole(s) extraction. Each of these steps is described below. Note that polygon extraction is independent of the specific triangular mesh regions  $\mathcal{T}_{r,i}$ , thus subsequent notation will drop the  $i$  index for brevity when used in algorithms.

1) *Data structure initialization*: Data structure initialization is shown in Algorithm 2 which produces three data structures: a boundary half-edge set, a point index hash map, and the extreme point. A visual example of these data structures is shown in Figure 4. Boundary half-edge set  $\mathcal{HE}$  contains the half-edge indexes that are on the exterior border, marked in blue in Figure 4a. A half-edge is marked as a boundary if it has no opposite half-edge or if its adjacent triangle is not in  $\mathcal{T}_{r,i}$ .

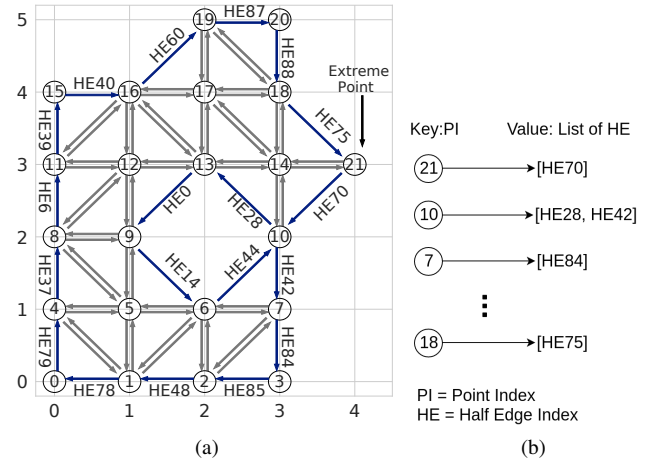


Fig. 4. (a) The boundary half-edge set is marked in blue and point index 21 (PI21), the farthest point on the x-axis, is noted. (b) A sample of the resulting point index hash map,  $PtE$  is shown.

The second data structure is a point index hash map,  $PtE$ , whose *key* is a point index and *value* is a *list* of outgoing boundary half-edges from the keyed point index. This hash map is represented in Figure 4b; note the keyed point index 21 mapping to the single element list containing half-edge 70. The final data structure represents an extreme point in the

---

**Algorithm 2:** Initialize

---

**Input :** Triangular Mesh Region ,  $\mathcal{T}_r = \{t_i, \dots, t_k\}$   
Shared Halfedges, *halfedges*  
Triangles Point Index, *triangles*  
**Output:** Half Edge Set ,  $\mathcal{HE} = \{he_i, \dots, he_n\}$   
Point Index Hash Map, *PtE*  
Extreme Point,  $pi_{xp}$

```
1  $\mathcal{HE} = \emptyset$ ; // boundary half-edge set
2  $PtE = \emptyset$ ; // Point to half-edge hashmap
3  $pi_{xp} = 0$ ; // will be overwritten
4 for  $t_i \in \mathcal{T}_r$  do
5   for  $he_i \in t_i$  do
6      $he_j = halfedges[he_i]$ ; // opposite edge
7      $t_j = floor(he_j/3)$ ; // adjacent tri
8     if  $t_j \notin \mathcal{T}_r$  then
9        $\mathcal{HE} = \mathcal{HE} + he_i$ ; // boundary edge
10       $pi = triangles[he_i]$ 
11       $pi_{xp} = TrackXp(pi, pi_{xp})$ 
12      if  $pi \notin PtE$  then
13        /* create half-edge list */
14         $PtE[pi] = [he_i]$ 
15      else
16        Append( $PtE[pi], he_i$ )
17    end
18 end
19 return  $\mathcal{HE}, PtE, pi_{xp}$ 
```

---

triangle mesh, referring to the point farthest to the right on the  $x$ -axis. Multiple points may exist on the extreme edge; the algorithm will track the first one found in this case.

2) *Concave Shell Extraction:* Outer shell extraction begins by traversing the half-edge graph, starting with the half-edge provided by the extreme point. As the edges are traversed the point indices are recorded in a list representing the linear ring of the concave hull. In Figure 4a the extreme point index is  $PI_{21}$  and the starting half-edge is  $HE_{70}$ . This starting half edge and start point index are arguments to the `ExtractLinearRing` procedure in Algorithm 3, with the procedure halting when edge traversal returns back to the starting point index, indicating a closed linear ring has been extracted. The hole in this shape, represented by edges ( $HE_{28}$ ,  $HE_0$ ,  $HE_{14}$ ,  $HE_{44}$ ), with a shared vertex at  $PI_{10}$ , must be carefully handled as explained below.

The example in Figure 4 begins with  $HE_{70}$  traversing to  $PI_{10}$ . The outgoing boundary half-edges for this point index are determined from  $PtE$  which provides a list of both  $HE_{28}$  and  $HE_{42}$ . However  $HE_{28}$  is an edge for a hole in this polygon while  $HE_{42}$  is the correct half-edge to traverse for the outer shell. The `SelectEdge` procedure determines which of these edges to choose and is visually outlined in Figure 5. Angles between the proposed edges and  $HE_{70}$  are calculated and the edge with the largest angle is chosen which guarantees the largest concave hull. This edge cannot be a hole edge because that would imply that the hole is outside the concave shell, which is invalid.

---

**Algorithm 3:** ExtractLinearRing

---

**Input :** Half Edge Set ,  $\mathcal{HE} = \{he_i, \dots, he_n\}$   
Point Index Hash Map, *PtE*  
Starting half-edge, *he*  
Start point index, *startPI*  
Triangles Point Index, *triangles*  
**Output:** Linear Ring ,  $lr = [pi_1, \dots, pi_k]$

```
1  $lr = []$ ; /* empty linear ring */
2 while True do
3    $\mathcal{HE} = \mathcal{HE} \setminus he$ 
4    $he_t = NextTriangleEdge(he)$ 
5    $pi = triangles[he_t]$ 
6   Append( $lr, pi$ )
7   if  $pi$  is startPI then
8     /* closed linear ring */
9     break
10     $nextEdges = PtE[pi]$ 
11     $he = SelectEdge(he, nextEdges)$ 
12 end
13 return  $lr$ 
```

---

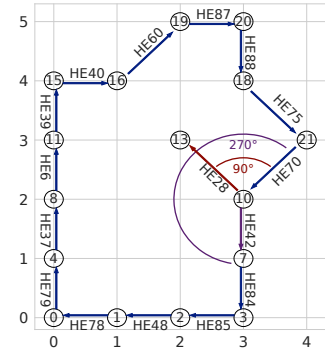


Fig. 5. Edge selection for Fig. 4a.  $HE_{70}$  leads to point index  $PI_{10}$  during shell extraction. Half-edges  $HE_{28}$  and  $HE_{42}$  leave  $PI_{10}$ . The correct edge to follow ( $HE_{42}$ ) has the greatest angle with  $HE_{70}$ .

3) *Hole(s) Extraction:* After the outer shell of the concave hull has been determined, only the holes remain to be found (if any holes exist). Any edges that remains inside  $\mathcal{HE}$  are hole edges and will be extracted using Algorithm 4. A half-edge is randomly chosen from  $\mathcal{HE}$  for which the same `ExtractLinearRing` procedure is run. Figure 6a shows a corner case that must be handled if two holes share the same vertex. The previously extracted concave shell is displayed in green while the remaining half-edges to be processed are in blue; note the shared vertex at  $PI_{16}$ . Figure 6b shows the event when  $HE_{19}$  is randomly chosen for hole extraction leading to  $PI_{16}$ .  $HE_0$  or  $HE_{29}$  is chosen in the manner previously discussed: the edge with largest angle guarantees the smallest hole thus is chosen. If the other edge was chosen this would indicate a hole inside a hole which is invalid.

### E. Time Complexity

This section describes the time complexity of PolyLidar. The Delaunay triangulation is first computed in  $\mathcal{O}(n \log n)$

**Algorithm 4: Extract Holes**


---

**Input** : Half Edge Set ,  $\mathcal{HE} = \{he_i, \dots, he_n\}$   
Point Index Hash Map,  $PtE$   
Triangles Point Index,  $triangles$

**Output:** Set of Linear Ring Holes ,  
 $\mathcal{HR} = \{lr_1, \dots, lr_k\}$

- 1  $\mathcal{HR} = \emptyset$  ; /\* empty hole set \*/
- 2 **while**  $\mathcal{HE}$  is not empty **do**
- 3      $he = \text{RandomChoice}(\mathcal{HE})$
- 4      $pi = triangles[he]$
- 5      $lr =$   
        $\text{ExtractLinearRing}(\mathcal{HE}, PtE, he, pi, triangles)$
- 6      $\mathcal{HR} = \mathcal{HR} + lr$
- 7 **end**
- 8 **return**  $\mathcal{HR}$

---

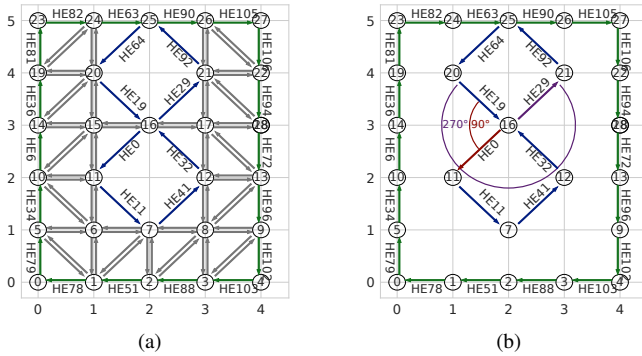


Fig. 6. (a) Edge case of two holes sharing the same vertex at PI16. The outer shell (green) is already extracted. (b) When traversing from HE19 to point index PI16, two outgoing edges (HE0 and HE29) are found. Edge HE29 with the largest angle difference from HE19 is chosen.

[20]. Region extraction from Section IV-C is  $\mathcal{O}(n)$ :

- At most  $t = 2n - 2$  triangles are returned from Delaunay triangulation by Euler's formula so  $t$  is linear in  $n$ .
- The maximum of  $2 * t$  iterations occurs. One loop filters triangles; worst case no triangles are removed. A second loop occurs over remaining connected triangles.
- Determining shared edges for expansion requires an  $\mathcal{O}(1)$  lookup in the *halfedges* array.
- Output generation  $\mathcal{T}_r$  is  $\mathcal{O}(1)$  for each insertion.

Polygon extraction is also  $\mathcal{O}(n)$ . The initialization procedure in Algorithm 2 is  $\mathcal{O}(n)$  per the following analysis:

- Assuming the worst case, the algorithm loops through every edge of every triangle, providing a maximum number of iterations of  $3 \cdot t$ . Therefore the number of iterations is linear with  $n$ .
- Determining if an edge is a boundary edge is an  $\mathcal{O}(1)$  operation. Line 6 is  $\mathcal{O}(1)$  lookup in *halfedges* array. Line 8 is  $\mathcal{O}(1)$  lookup in the input triangle set.
- Output generation, the half-edge set and point index hash map, is  $\mathcal{O}(1)$  for each insertion.

Algorithm 3 is linear in  $n$  for similar reasons:

- The number of iterations is the number of boundary

edges computed, a subset of the iterations in Alg. 2.

- The output linear ring is  $\mathcal{O}(1)$  for each insertion.
- The *SelectEdge* procedure is  $\mathcal{O}(1)$  with no loops.

Finally Algorithm 4 is also linear with respect to  $n$ . It is executed as many times as there are holes in a polygon. A hole contains a minimum of one triangle; we have shown previously that  $t$  grows linearly with  $n$ . Selecting a random half-edge, Line 3, is an  $\mathcal{O}(1)$  operation. Overall, PolyliDar has complexity  $\mathcal{O}(n \log n)$  from the initial triangulation.

## V. BENCHMARKING COMPARISONS

This section benchmarks PolyliDar against other common concave hull extraction methods which also extract holes; all code is open source<sup>1</sup>. Three other implementations are tested: CGAL's alpha shape function and the *ST\_ConcaveHull* function from PostGIS and Spatialite. For uniformity, PolyliDar and CGAL are set to use the same  $\alpha$  parameter to guarantee exact shape reproduction. Note that CGAL's alpha shape function returns an unordered set of edges; it does not convert these edges into a valid (multi)polygon. These edges produce the same shape as PolyliDar when drawn on a canvas, but lack the desired polygon semantic data structure. However we show that PolyliDar still outperforms CGAL in time. PostGIS's concave hull implementation only returns single polygons, so MultiPolygon test cases are not evaluated against it. Both PostGIS and Spatialite are databases which require upload of the point set prior to algorithm execution; benchmark timing does not include data upload time. PolyliDar is configured to use fast adaptive precision floating point arithmetic for robust geometric predicates using [21].

Section V-A will use the state shapes of California (CA) and Hawaii (HI) as test cases to explore how the algorithms scale with respect to point size. Section V-B comprehensively evaluates each algorithm for the 26 letters in the English alphabet (transformed to polygons), similarly to [11]. Both sections use the test case as a ground truth (multi)polygon shape,  $GT$ , from which a 2D point set is uniformly sampled. Each implementation takes as input this point set and produces a concave shape,  $CS$ , which is similar to the ground truth polygon. The  $L^2$  error norm, the area of the symmetric difference between  $GT$  and  $CS$ , is computed to enable evaluation of shape area error  $\frac{area((GT-CS) \cup (CS-GT))}{area(CS)}$ .

Each implementation contains its own parameter(s) modified to provide good results, i.e., minimize  $L^2$  error. Shape accuracy is therefore subject to parameter selection. Table II displays the parameters chosen and used for all three test cases (CA, HI, and all 26 letters in alphabet). Rows with two parameters separated by a semicolon indicate parameters for use with non-hole and hole cases. PolyliDar and CGAL use the same  $\alpha$  parameter adjusted on a case by case basis. For each case we calculate point density  $p_d$  and compute parameter  $\alpha$  as  $2p_d^{-1}$ . This gives reasonable but not necessarily optimal results. Spatialite's concave hull implementation has parameter  $C$  which at its default value ( $C = 3$ ) produces excellent results.  $C$  is adjusted as needed

<sup>1</sup><https://github.com/JeremyBYU/concavehull-evaluation>

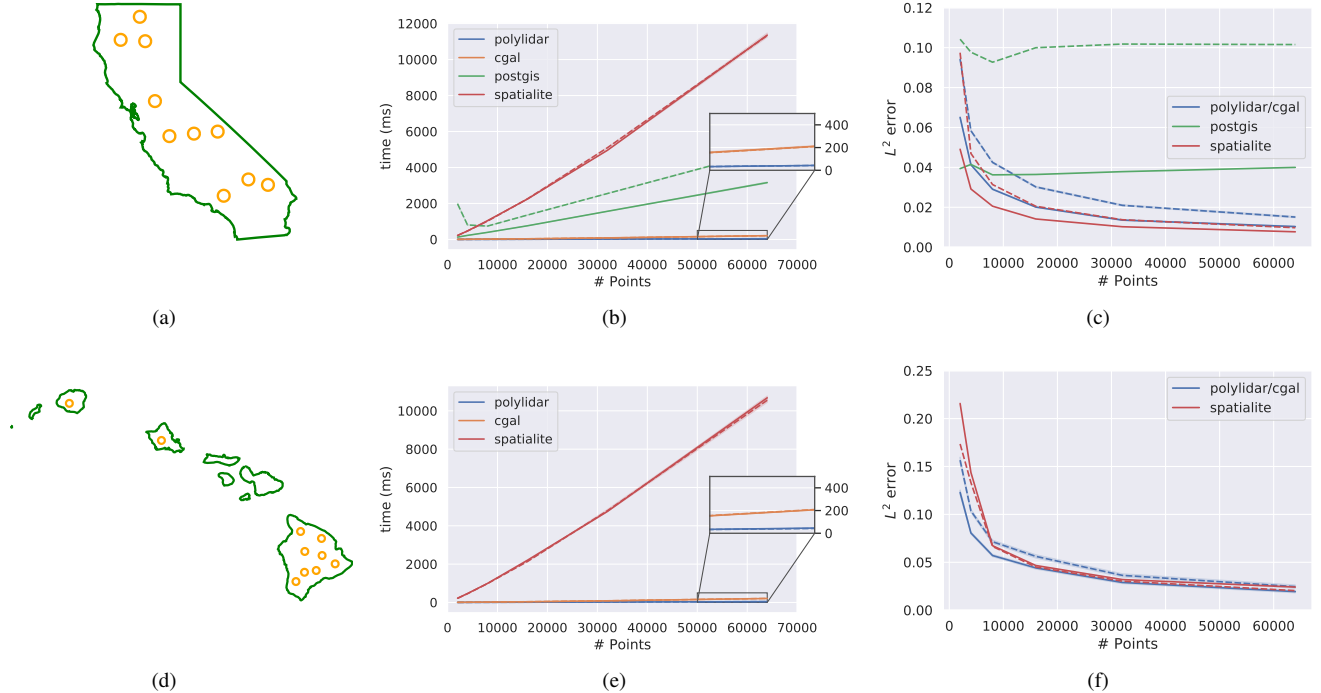


Fig. 7. Concave hull extraction results. Rows from top to bottom correspond to outlines of California (CA) (a, b, c), and Hawaii (HI) (d, e, f) with random holes inserted. The first column shows ground truth polygons with circular holes in orange. The second column shows execution time as a function of number of 2D points provided. The third column shows shape error as a function of number of 2D points provided. Dashed lines show results where holes were placed inside the polygon outline, while solid lines show results with no holes. PostGIS cannot handle MultiPolygons thus was not tested for HI.

(for CA, HI) to further reduce error. PostGIS’ *target percent* is set to provide the optimal accuracy based on percent area reduction required. The most important takeaway when interpreting accuracy graphs is thus trends in accuracy, not small numerical differences.

TABLE II  
PARAMETERS FOR TEST CASES

Algorithm	Parameter Name	CA	HI	Alphabet
CGAL/Polylidar	$\alpha$	$2p_d^{-1}$	$2p_d^{-1}$	$2p_d^{-1}$
Spatialite	$C$	2	2.0;1.25	3
PostGIS	<i>target percent</i>	0.76;0.72	-	Varies

### A. State Shapes

Figure 7 shows CA and HI test case geometries (first column), execution times (second column), and error results (third column). Each state shape is processed with and without random holes to verify each implementation’s ability to handle hole extraction. Dashed lines indicate results where holes are included in the ground truth polygon. Each test was run 10 times with input point set sizes ranging from (2, 4, 8, 16, 32, 64) thousand points with mean timing and error plotted. Confidence intervals are provided for execution timing, however they are almost imperceptible because the variance is low at this scale. Polylidar and CGAL are significantly faster than the other methods, with Spatialite having the slowest implementation. An inset (zoomed) box

that focuses solely on CGAL and Polylidar is shown in the second column, showing that on average Polylidar is  $\sim 4$  times faster than CGAL. Spatialite’s slow speed is attributed to unioning triangles to determine final polygon shape as determined through profiling [22]. The presence of holes affected each method differently: decreased time in Spatialite (fewer triangles to union), increased time for PostGIS (a decrease in *target percent* increases run-time). No significant changes were noted for CGAL and Polylidar.

Polylidar and CGAL are configured to produce the same shape and therefore have the same  $L^2$  error. Spatialite produced shapes with the least error, followed by Polylidar/CGAL and then PostGIS. Spatialite’s low error is due to filtering based on triangle edge length statistics. PostGIS error increased markedly with holes because it did not accurately reproduce them. Figure 8 shows a visual comparison of CA concave polygon outputs for each algorithm.

### B. Alphabet Shapes

Ground truth polygons were generated from 26 capital letters of the English alphabet. Some polygon letters naturally have holes such as “A”, however no capital letters are MultiPolygons. Each letter was uniformly sampled to generate a 2000 point set and run through each algorithm. The “A” in Figure 1b shows an example capital letter with the output of Polylidar’s concave hull. Table III provides aggregate statistics of all 26 test cases.

Polylidar continues to lead in speed, about 4.5 times faster than the next leading algorithm CGAL (shape error remains

TABLE III  
ALPHABET LETTER RESULTS, 26 SHAPES

Algorithm	$L^2$ error %			Time (ms)		
	mean	std	max	mean	std	max
polylidar	12.8	1.8	16.8	1.2	0.3	2.4
cgal	12.8	1.8	16.8	5.4	0.9	7.2
postgis	36.5	9.9	53.7	13091.8	7500.6	28451.0
spatialite	11.2	4.5	22.1	230.2	6.3	242.9

the same because of same  $\alpha$  used). Spatialite continues to lead in accuracy by a marginal amount for the same reasons discussed previously. However PostGIS shape error and time are significantly higher than previously seen. This is because the alphabet shapes are significantly more concave than the tested state shapes, requiring a much smaller *target percent* parameter for PostGIS (on average 0.38). Documentation of PostGIS indicates that the run time grows quadratically when reducing this parameter and at “small” values may fail to produce a concave shape [15]. PostGIS failed to produce any shape for the letters “J”, “L”, and “M”. All other algorithms provided valid results for all test cases.

## VI. RANDOM POLYGON TESTS

More than 19,600 polygons were randomly generated to test PolyLidar. Half the test cases had random holes. Polygon complexity is characterized by convexity metric

$$CV = \frac{Area(P)}{Area(CH(P))}$$



Fig. 8. Concave polygon output from PolyLidar/CGAL (left), Spatialite (center), and PostGIS (right). Input to each algorithm was a 4000 point set sampled from the California (CA) polygon with holes per Figure 7d.

where  $P$  is the polygon and  $CH()$  is the convex hull function. A convexity of 1 indicates the sample polygon is its convex hull. Point sets of size 2,000 and 8,000 were uniformly sampled for each polygon and input to PolyLidar with the  $\alpha$  parameter from Table II. Execution time and accuracy are summarized in Table IV. The table is partitioned into high, medium, and low ground truth polygon convexity defined by  $CV \geq 0.75$ ,  $0.75 < CV \leq 0.55$ , and  $CV < 0.55$  respectively. Figure 9 illustrates the impact of  $CV$  value on polygon shape. Note that the CA polygon has a  $CV = 0.74$ . Every polygon produced by PolyLidar (39,200) was confirmed valid independently by the GEOS spatial library. In all examples we find that greater point density improves PolyLidar accuracy. Also, as polygon convexity ( $CV$ ) decreases PolyLidar shape estimation accuracy also decreases.

Polygons in our “low” convexity class have extremely non-convex shapes, the lowest with  $CV = 0.26$  per Figure 9.

TABLE IV  
RANDOM TESTS;  $CV =$  CONVEXITY METRIC

$CV$	points	$L^2$ error %			Time (ms)		
		mean	std	max	mean	std	max
hi	2000	8.4	1.0	11.6	1.1	0.0	1.5
	8000	4.4	0.5	6.1	4.6	0.1	5.0
mid	2000	15.1	2.0	23.7	1.1	0.0	1.7
	8000	8.0	1.1	13.0	4.6	0.1	8.1
low	2000	28.3	5.1	43.6	1.1	0.0	1.3
	8000	15.5	3.0	25.0	4.7	0.2	9.9

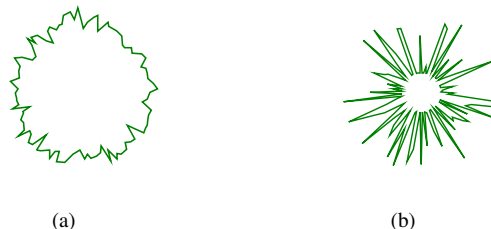


Fig. 9. (a) Example of a high convexity polygon;  $CV = 86.1\%$  (b) and a low convexity polygon;  $CV = 26.2\%$

## VII. CONCLUSION

This paper has introduced PolyLidar, an efficient 2D concave hull extraction algorithm which produces (multi)polygon output with holes. Comparison benchmarks of numerous test sets, similarly done in [11], show PolyLidar is faster than competing approaches with comparable or better accuracy. Additionally we perform random polygon tests that confirm every polygon produced by PolyLidar is valid. In future work we will extend PolyLidar with a filter similar to that found in Spatialite to reduce the need for manual parameter tuning. We will explore parallelism to further increase speed and will extend PolyLidar to operate on 3D point cloud data.

## REFERENCES

- [1] W. Hess, D. Kohler, H. Rapp, and D. Andor. Real-time loop closure in 2d lidar slam. In *2016 IEEE International Conference on Robotics and Automation (ICRA)*, pages 1271–1278, May 2016.
- [2] S. Malihi, M. J. Valadan Zoej, M. Hahn, M. Mokhtarzade, and H. Arefi. 3D Building Reconstruction Using Dense Photogrammetric Point Cloud. *Intl. Archives of the Photogrammetry, Remote Sensing and Spatial Inf. Sciences*, pages 71–74, Jun 2016.
- [3] M. Himmelsbach, F. v. Hundelshausen, and H.-J. Wuensche. Fast segmentation of 3d point clouds for ground vehicles. In *2010 IEEE Intelligent Vehicles Symposium*. IEEE, 2010.
- [4] J.N. Bakambu, P. Allard, and E. Dupuis. 3d terrain modeling for rover localization and navigation. In *The 3rd Canadian Conference on Computer and Robot Vision (CRV06)*. IEEE, 2006.
- [5] David Gingras, Tom Lamarche, Jean-Luc Bedwani, and Érick Dupuis. Rough terrain reconstruction for rover motion planning. In *2010 Canadian Conference on Computer and Robot Vision*. IEEE, 2010.
- [6] Shaogang Jin, Jiyang Zhang, Lincheng Shen, and Tengxiang Li. On-board vision autonomous landing techniques for quadrotor: A survey. In *35th Chinese Control Conf.*, pages 10284–10289. IEEE, 2016.

- [7] H. Oleynikova, D. Honegger, and M. Pollefeys. Reactive avoidance using embedded stereo vision for mav flight. In *IEEE Intl. Conf. on Robotics and Auto. (ICRA)*, May 2015.
- [8] J. Castagno, C. Ochoa, and E. Atkins. Comprehensive risk-based planning for small unmanned aircraft system rooftop landing. *Intl. Conf. on Unmanned Aircraft Sys.*, 2018.
- [9] J. Castagno and E. Atkins. Roof shape classification from lidar and satellite image data fusion using supervised learning. *Sensors*, 2018.
- [10] Github - polylidar. <https://github.com/JeremyBYU/polylidarv2>, 2019. Accessed: 2019-01-05.
- [11] M. Duckham, L. Kulik, M. Worboys, and A. Galton. Efficient generation of simple polygons for characterizing the shape of a set of points in the plane. *Pattern Recognition*, 41(10):3224–3236, 2008.
- [12] H. Edelsbrunner, D. Kirkpatrick, and R. Seidel. On the shape of a set of points in the plane. *IEEE Transactions on Information Theory*, 29(4):551–559, July 1983.
- [13] A. Furiere. Spatialite. <https://www.gaia-gis.it/fossil/libspatialite/index>, 2017. Visited on 2017-01-14.
- [14] D. Chen, X. Han, and W. Wang. Use of sqlite on embedded system. In *Intl. Conf. on Intel. Comp. and Cognitive Inform.* IEEE, 2010.
- [15] OSGeo. Postgis. [https://postgis.net/docs/ST\\_ConcaveHull.html](https://postgis.net/docs/ST_ConcaveHull.html), 2019. Visited on 2019-01-14.
- [16] The CGAL Project. *CGAL User and Reference Manual*. CGAL Editorial Board, 4.14 edition, 2019.
- [17] John R Herring. Opengis implementation specification for geographic information-simple feature access-part 1: Common architecture. *Open Geospatial Consortium*, page 95, 2006.
- [18] Github - delaunator. <https://github.com/mapbox/delaunator>, 2018. Accessed: 2018-01-05.
- [19] Rujun Cao, Yongjun Zhang, Xinyi Liu, and Zongze Zhao. Roof plane extraction from airborne lidar point clouds. *International Journal of Remote Sensing*, 38(12):3684–3703, 2017.
- [20] M. de Berg, O. Cheong, M. van Kreveld, and M. Overmars. Delaunay triangulations: height interpolation. *Computational Geometry: Algorithms and Applications*, pages 191–218, 2008.
- [21] Jonathan Richard Shewchuk. Adaptive precision floating-point arithmetic and fast robust geometric predicates. *Discrete & Computational Geometry*, 18(3):305–363, 1997.
- [22] Github - google pprof. <https://github.com/google/pprof>, 2019. Accessed: 2019-01-05.